Nano Research 2016, 9(4): 951–962
DOI 10.1007/s12274-016-0983-3
Research Article

ISSN 1998-0124
CN 11-5974/O4

Rational synthesis of carbon shell coated polyaniline/MoS_2 monolayer composites for high-performance supercapacitors

Chao Yang[1], Zhongxin Chen[1], Imran Shakir[2], Yuxi Xu[1] (✉), and Hongbin Lu[1] (✉)

[1] *State Key Laboratory of Molecular Engineering of Polymers, Department of Macromolecular Science, Collaborative Innovation Center of Polymers and Polymer Composite Materials, Fudan University, Shanghai 200433, China*

[2] *Sustainable Energy Technologies (SET) center College of Engineering, King Saud University, PO-BOX 800, Riyadh 11421, Kingdom of Saudi Arabia*

Received: 8 November 2015
Revised: 16 December 2015
Accepted: 18 December 2015

KEYWORDS

supercapacitor,
polyaniline,
molybdenum disulfide,
carbon shell,
cycle stability

ABSTRACT

Conducting polymers generally show high specific capacitance but suffer from poor rate capability and rapid capacitance decay, which greatly limits their practical applications in supercapacitor electrodes. To this end, many studies have focused on improving the overall capacitive performance by synthesizing nanostructured conducting polymers or by depositing a range of coatings to increase the active surface area exposed to the electrolyte and enhance the charge transport efficiency and structural stability. Despite this, simultaneously achieving high specific capacitance, good rate performance, and long cycle life remains a considerable challenge. Among the various two-dimensional (2D) layered materials, octahedral (1T) phase molybdenum disulfide (MoS_2) nanosheets have high electrical conductivity, large specific surface areas, and unique surface chemical characteristics, making them an interesting substrate for the controlled growth of nanostructured conducting polymers. This paper reports the rational synthesis of carbon shell-coated polyaniline (PANI) grown on 1T MoS_2 monolayers (MoS_2/PANI@C). The composite electrode comprised of MoS_2/PANI@C with a ~3 nm carbon shell exhibited a remarkable specific capacitance of up to 678 $F \cdot g^{-1}$ (1 $mV \cdot s^{-1}$), superior capacity retention of 80% after 10,000 cycles and good rate performance (81% at 10 $mV \cdot s^{-1}$) due to the multiple synergic effects between the PANI nanostructure and 1T MoS_2 substrates as well as protection by the uniform thin carbon shell. These properties are comparable to the best overall capacitive performance achieved for conducting polymers-based supercapacitor electrodes reported thus far.

Address correspondence to Yuxi Xu, xuyuxi@fudan.edu.cn; Hongbin Lu, hongbinlu@fudan.edu.cn

1 Introduction

Over the last decade, supercapacitors (SCs) have attracted considerable research attention with the ever-increasing energy demand and impending energy crisis [1–3]. Pseudocapacitors are one of the most promising energy storage devices because of their combination of high power density, high energy density, and long cycle life [4–6]. Unfortunately, the electrodes currently in use for pseudocapacitors do not meet application requirements. Therefore, tremendous efforts have been made to synthesize high-performance, inexpensive, and earth-abundant materials, such as metal-organic frameworks, single-layered hydroxide, three-dimensional hybrids, and conjugated microporous polymers [7–12]. Among the various pseudocapacitive electrode materials, conducting polymers such as polyaniline (PANI) are quite attractive on account of their much higher theoretical specific capacitance compared to carbon-based electrodes, low cost, small environmental impact, and ease of fabrication for large-scale devices [13–15]. However, they often suffer from severe performance fading after cycling up to 1,000 times due to swelling and shrinkage of the bulk polymers and subsequent mechanical degradation during the doping and de-doping of ions [16–18]. A possible solution to this challenge is to coat the polymer nanostructures with a thin layer, such as Nafion [19], graphene [20], novel metal oxide [18], transition metal oxide [21], or other polymers [22]. However, the poor electrical conductivity, large charge transfer resistance and the rarity of noble metals largely reduce the capacitance, cycling stability, and potential applications of conducting polymer electrodes. In practice, achieving high specific capacitance combined with good cycle stability (e.g., over 10,000 cycles) remains a challenge for most conducting polymer-based SCs. This is due primarily to the inherent volume expansion of conducting polymers during the charge–discharge process. On the other hand, it is also related to the reduced charge transfer efficiency of the polymer nanostructures [23, 24].

Recently, molybdenum disulfide (MoS_2) has been evaluated for use in electrochemical storage [25–29]. In contrast to the semiconductive trigonal prismatic (2H) phase with a bandgap of ~1.9 eV, which makes it less attractive as an electrode material, octahedral (1T) phase MoS_2 is hydrophilic with a more than 100 times higher conductivity than the 2H phase, exhibiting excellent electrochemical properties [30, 31]. MoS_2 containing 70% 1T phase can even achieve a capacitance of 400–700 $F \cdot cm^{-3}$ by intercalating and accumulating ions [27]. Moreover, the synergic effects arising from the intense interfacial coupling between the monolayer MoS_2 nanosheets (NSs) and polymer nanostructures help enhance the capacitive performance of the polymer composites electrode [28]. This highlights the potential of 1T-phase MoS_2 for the efficient integration of conducing polymers for achieving high-performance electrode materials of SCs with high specific capacitance and long cycle stability. Nevertheless, these remain to be realized because most studies reported either a low specific capacitance or poor cycling stability.

This paper reports a simple method for producing hierarchical nanohybrids by depositing PANI directly on MoS_2 monolayers containing 72% 1T phase followed by a carbon shell coating with a controlled thickness. The composite electrode with the carbon-coated PANI on MoS_2 exhibited a remarkable capacitance of up to 678 $F \cdot g^{-1}$ due to the multiple synergic effects between PANI and MoS_2 as well as the thin carbon coating, and superb cycle stability (80%) after 10,000 cycles. This makes it among the best conducting polymer-based electrode materials reported thus far. The procedure for synthesizing MoS_2/PANI@C composites is illustrated in Scheme 1. First, MoS_2 monolayers were produced

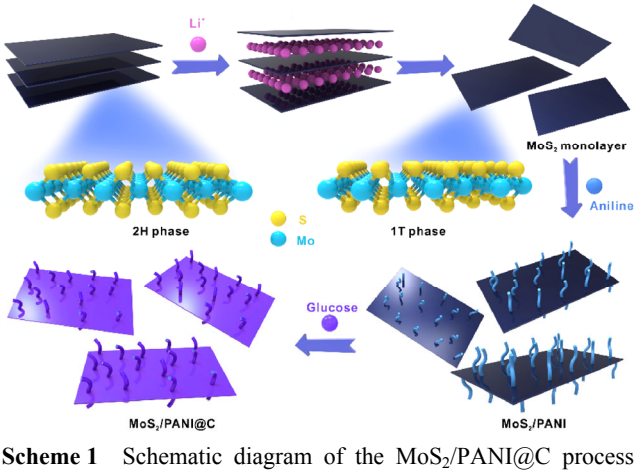

Scheme 1 Schematic diagram of the MoS_2/PANI@C process for the synthesis of carbon-encapsulated PANI based on MoS_2 monolayer NSs.

using a previously reported Li-intercalation and sonication-assisted exfoliation method. Subsequently, the polymerization of aniline took place on the surface of the MoS_2 monolayers using ammonium persulfate (APS) as the initiator under acidic conditions, which facilitated a uniform, high loading of PANI. After the reaction for 10 h, the mixture was added to an aqueous solution of glucose to form a thin carbon layer on MoS_2/PANI by a hydrothermal treatment (see Experimental Section).

2 Experimental

2.1 Synthesis of chemical exfoliated MoS_2

Chemically exfoliated MoS_2 was synthesized by lithium intercalation into bulk MoS_2 powder, as reported elsewhere (see the ESM for experimental details) [27].

2.2 Synthesis of PANI deposited on MoS_2 monolayer NSs (MoS_2/PANI)

The monolayer MoS_2 NSs solution and aniline were added to a 0.5 M HCl solution with a weight ratio of 1:20.0 (MoS_2 NSs:aniline). The mixture was then ultrasonicated for 10 min. The uniform mixture was stirred while cooling in a NaCl ice bath (–3 to –5 ℃). At the same time, APS in a 0.5 M HCl solution with a molar ratio of 1:2 (APS:aniline) was added dropwise as an initiator to induce the polymerization of aniline. The dark green product that formed after the reaction for 10 h was washed sequentially with water (3 × 100 mL) and ethanol (2 × 100 mL) while filtering. The as-prepared product was called MoS_2/PANI-I. For comparison, MoS_2/PANI-II and MoS_2/PANI-III were also synthesized with a weight ratio of 1:13.3 and 1:33.4 (MoS_2 NSs:aniline), respectively, under the same conditions. Pure PANI nanowires (NWs) were prepared under the same conditions except for the use of de-ionized water as the solvent without the addition of a MoS_2 NSs solution.

2.3 Deposition of the carbonaceous shell onto MoS_2/PANI

A uniform carbon shell was deposited onto the as-prepared MoS_2/PANI-I by a hydrothermal reaction using glucose as the carbon precursor. MoS_2/PANI-I and a glucose solution with a weight ratio of 1:26.3 (MoS_2/PANI-I:glucose) were transferred to a Teflon lined stainless steel autoclave. The autoclave was heated to 160 ℃ in an electric oven for 2 h and allowed to cool to room temperature. The mixture was filtered, rinsed with DI water and dried in air. The carbon coated MoS_2/PANI-I was called MoS_2/PANI-I@C-3nm. For comparison, a carbonaceous shell was deposited on MoS_2/PANI-II and MoS_2/PANI-III under the same conditions as MoS_2/PANI-I; the products were called MoS_2/PANI-II@C-3nm and MoS_2/PANI-III@C-3nm, respectively. MoS_2/PANI-I@C with different carbonaceous shell thicknesses were synthesized using the same hydrothermal method for 4 h and with a weight ratio of 1:(6 × 26.3) (MoS_2/PANI-I:glucose) (denoted as MoS_2/PANI-I@C-5nm and MoS_2/PANI-I@C-9nm, respectively).

2.4 Characterization

Atomic force microscopy (AFM) was performed using a Multimode Nano 4 in tapping mode. The samples for the AFM observations were prepared by depositing the exfoliated MoS_2 NSs onto clean SiO_2/Si surfaces. Transmission electron microscopy (TEM, Tecnai G2 F20 Twin, operating at 200 kV) was used to observe the morphology of the samples. Gold particles were deposited by sputtering (Q150R, Quorum Tech. Ltd.) with a current of 5 mA for 150 s before determining the thickness of the carbonaceous shell by TEM. All samples for imaging were prepared by depositing the ethanol dispersions on holey copper grids. X-ray diffraction (XRD, PANalytical X'Pert PRO) was carried out using Cu Kα radiation (λ = 1.54 Å) in the 2θ range, 5° to 80°, operating at 40 kV and 40 mA. Field-emission scanning electron microscopy (FESEM, Ultra 55) was used to observe the morphology of the samples. Fourier transform infrared spectroscopy (FTIR) was recorded on a NEXUS 6700 spectrometer with a resolution of 2 cm^{-1} in the range, 400 to 4,000 cm^{-1}. The Raman shifts were confirmed by Raman spectroscopy (excitation wavelength: 638 nm, XploRA, HORIBA JobinYvon). Zetasizer Nano analyzer (ZS90, Malvern Instruments) was used to measure the Zeta potential and size. X-ray photoelectron spectroscopy (XPS) was performed using an AXIS Ultra DLD spectrometer (Kratos Analytical Ltd.) and Φ04-500 (Perkin-Elmer).

2.5 Electrochemical characterization

A three-electrode configuration was used for cyclic voltammetry (CV) and the galvanostatic charge/discharge (GCD) measurements in a 1 M aqueous H_2SO_4 solution as the electrolyte, where a woven stainless steel mesh including the active material was used as the working electrode, an Ag/AgCl (in 3 M KCl) electrode as the reference electrode and a graphite rod (~5 mm diameter) as the counter electrode. The working electrode was prepared by mechanically mixing the active material powders, Super P® Li (TIMCAL) and polyvinylidene fluoride (PVDF, Sigma-Aldrich) binder with a weight ratio of 75:15:10. The mixture was then ground, and a small amount of N-methylpyrrolidone (NMP) was added to improve the homogeneity. Finally, the mixture was pressed on a woven stainless steel mesh at 10 MPa and then dried for 8 h in a vacuum oven at room temperature. The mass loading of the electrode was 1.2 mg·cm^{-2}. Electrochemical impedance spectroscopy (EIS) was performed over the range, 0.01 Hz to 10,000 kHz, at the open circuit potential with a perturbation of 5 mV. ZsimpWin software was used to fit the EIS data and obtain the parameters for the equivalent circuit 4 elements. A cycling stability test was conducted at a scan rate of 100 mV·s^{-1} for 10,000 cycles; 20 cycles were conducted in advance before each measurement.

3 Results and discussion

The AFM image in Fig. 1(a) shows that the MoS_2 bulk had been exfoliated into ~1 nm thick monolayers [32]. The lateral size of the exfoliated MoS_2 monolayers ranged from 100 to 500 nm, as shown in the TEM images (Fig. 1(b)). The hexagonal symmetric selected area electron diffraction (SAED) patterns indicated that these MoS_2 monolayers exhibited good crystallinity [33], as shown in the inset in Fig. 1(b). The restacked MoS_2 film displayed an additional (001) XRD peak at $2\theta = 8.7°$, which was different from that of the bulk MoS_2 shown in Fig. 1(c), together with peaks for the (002), (003), (004), and (005) planes. This indicates that

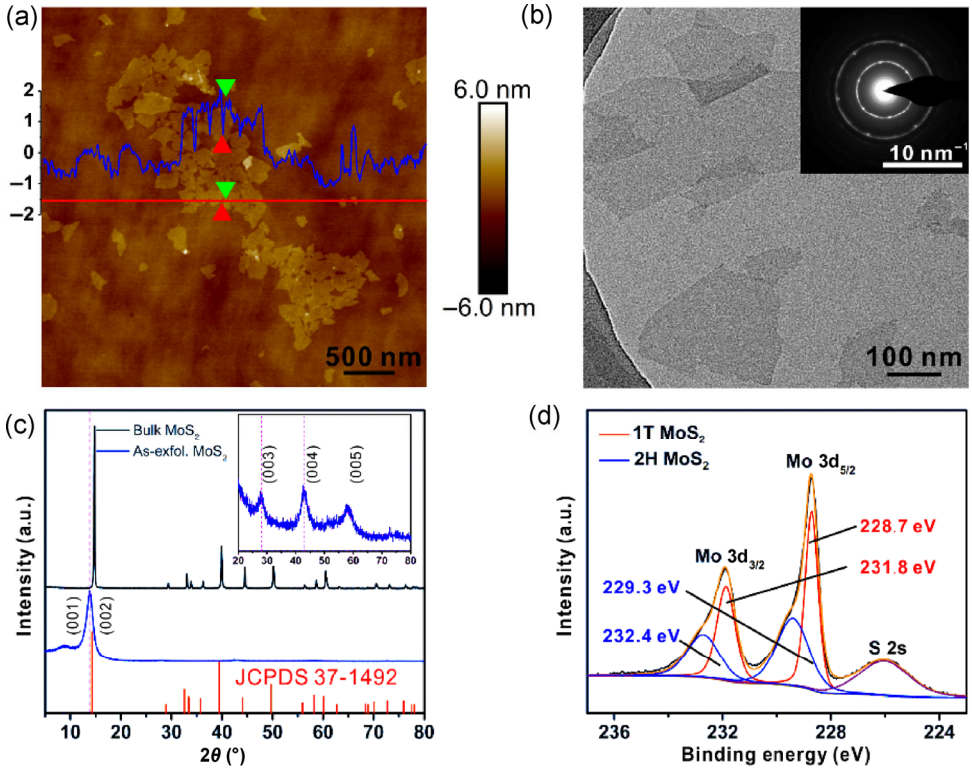

Figure 1 (a) AFM image and (b) TEM image of the monolayer MoS_2 NSs with the SAED image inserted. (c) XRD patterns of bulk MoS_2 and MoS_2 monolayer. The XRD pattern of the MoS_2 monolayer at $2\theta = 20°$~$80°$ is in the inset. (d) High-resolution XPS spectrum of Mo 3d of the MoS_2 monolayer.

the exfoliated monolayers are stacked randomly, with large interlayer spacings [27, 34]. A zeta potential of –40 mV indicated that these monolayers were negatively charged and contained a significant metallic 1T phase (Fig. S1 in the Electronic Supplementary Material (ESM)) [35]. The additional peaks in the Raman spectrum of MoS_2 (Fig. S2 in the ESM) also showed a single layer 1T MoS_2. The absence of a characteristic peak around 236 eV in the Mo 3d spectrum (Fig. 1(d)) indicated that the oxidation of Mo had been minimized. The S 2p spectrum (Fig. S3 in the ESM) confirmed that the monolayers contained up to 72% of the 1T phase [36].

The high specific area and high 1T phase content of the exfoliated MoS_2 monolayers make them ideal 2D substrates for the heterogeneous polymerization and uniform growth of PANI. The TEM images of MoS_2/PANI-I (at a weight ratio of 20.0∶1 (aniline to MoS_2), section 2.2) (Fig. 2(a)) and MoS_2/PANI-I@C-3nm (coated ~3 nm carbon shell by a hydrothermal treatment of MoS_2/PANI-I, section 2.3) (Fig. 2(b)) show that PANI grew intimately on the MoS_2 monolayers. By comparison, the pure PANI NWs were random net-like agglomerates (Fig. 2(c)). Such nanostructures were further confirmed by FESEM, FTIR spectroscopy and Raman spectroscopy, as shown in Figs. S4 and S5 in the ESM.

To observe the thickness of the coated carbon layers, gold nanoparticles were sprayed over the MoS_2/PANI-I surface (Fig. 3(a)) before the hydrothermal treatment and a hydrothermal reaction was then carried out to form MoS_2/PANI@C (Figs. 3(b)–3(d)) with a well-defined boundary between the carbon shell and MoS_2/PANI. The thickness of the coated carbon layers could be controlled by adjusting the hydrothermal reaction time and the glucose concentration (see the ESM). A carbon layer with a thickness of ~5 nm (Fig. 3(c), MoS_2/PANI-I@C-5nm) and ~9 nm (Fig. 3(d), MoS_2/PANI-I@C-9nm) on MoS_2/PANI-I was achieved, while MoS_2/PANI-I@C-3nm (Fig. 3(b)) had a 3 nm-thick carbon layer. The introduction of a carbon layer was also confirmed by XPS, where the C=C content in MoS_2/PANI-I@C-3nm after a 2 h hydrothermal treatment was slightly higher than that of MoS_2/PANI-I without the carbon coating (Fig. S6 in the ESM). The Mo 3d, S 2p and N 1s spectra for MoS_2/PANI@C (Figs. 2(d)–2(f)) and MoS_2/PANI (Figs. S7(a)–S7(c) in the ESM) further suggest the good integration of PANI on the MoS_2

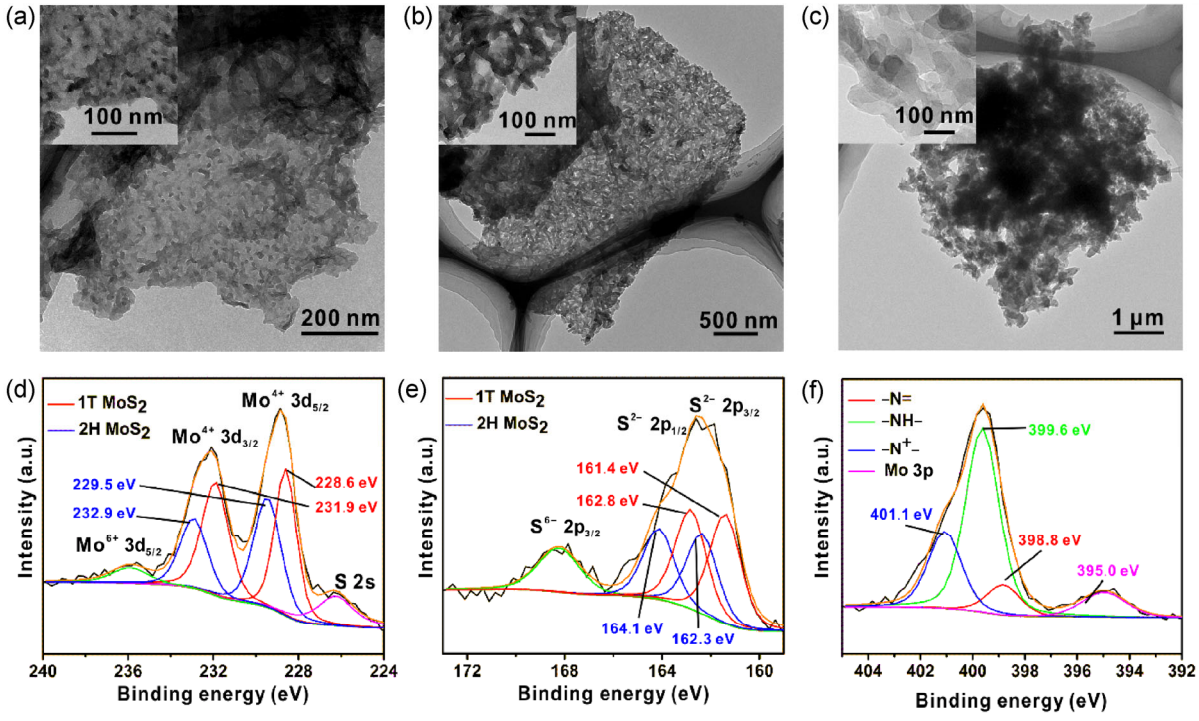

Figure 2 TEM images of (a) MoS_2/PANI-I, (b) MoS_2/PANI-I@C-3nm and (c) pure PANI nanowires, respectively. High-resolution XPS spectrum from (d) Mo 3d, (e) S 2p and (f) N 1s of MoS_2/PANI@C at the weight ratio of 2.0∶1 (aniline to MoS_2), respectively.

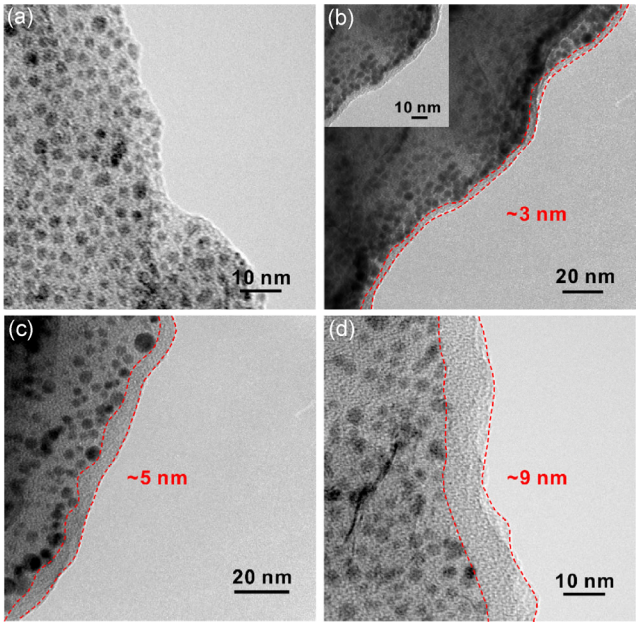

Figure 3 TEM images of (a) MoS_2/PANI-I, (b) MoS_2/PANI-I@C-3nm, (c) MoS_2/PANI-I@C-5nm and (d) MoS_2/PANI-I@C-9nm with different carbon coating thicknesses controlled by adjusting the hydrothermal time and glucose content: (a) 0 h, (b) 2 h, (c) 4 h and (d) 6 fold glucose.

monolayers, whereas for the MoS_2 monolayers, only slight oxidation was observed after the hydrothermal treatment (see the ESM text and Fig. S7 in the ESM).

The electrochemical performance of MoS_2/PANI-I@C-3nm was assessed using a three-electrode system. Figure 4(a) presents the typical CV curves with two pairs of obvious redox peaks for the MoS_2/PANI-I@C-3nm nanocomposite electrode over scan rates of 1–10 mV·s^{-1} in a 1 M H_2SO_4 electrolyte. The specific capacitance of MoS_2/PANI-I@C-3nm reached 678 F·g^{-1}, which is much higher than that of the pure PANI NWs (462 F·g^{-1}), MoS_2 (100 F·g^{-1}) (Fig. 5(a)) and most of the PANI-based electrodes reported previously (200–600 F·g^{-1}) [37–41], suggesting a synergic effect between the MoS_2 monolayers and PANI [42, 43]. Considering that the PANI content was approximately 41 wt.% (Fig. S8 and Table S1 in the ESM), the specific capacitance of PANI against its own weight was measured to be 1,650 F·g^{-1} at 1 mV·s^{-1}. When the scan rate was increased to 10 mV·s^{-1}, the capacitance of MoS_2/PANI-I@C-3nm still reached 549 F·g^{-1}, which is 81% capacitance retention compared to that at 1 mV·s^{-1}.

However, given the limited the diffusion time at high scan rates, to some extent, the electrolyte was unable to diffuse to the entire electrode surface for charge storage quickly and synchronously. Therefore, according to Eq. (1), the highest possible capacitance of the electrode should be constant with the sweep rate at low sweep rates [44, 45]. Figure 4(b) shows that the "total capacitance" was $Q_{v=0}$ = 746 F·g^{-1} when the scan rate approached 0 mV·s^{-1}. This suggests that only 9% of the capacitance is restricted by the limited ion diffusion at 1 mV·s^{-1}.

$$\frac{1}{Q_v} = \frac{1}{Q_{v=0}} + \text{constant}(v^{1/2}) \quad (1)$$

To further evaluate the performance of the electrode, GCD curves of MoS_2/PANI-I@C-3nm were measured at various current densities in a stable voltage window of 0.0–0.6 V (Fig. 4(c)). As shown in Fig. 4(d), the specific capacitance of MoS_2/PANI-I@C-3nm reached 668 F·g^{-1} at 1 A·g^{-1} and 479 F·g^{-1} at 10 A·g^{-1}, i.e., 72% retention, which is much higher than that reported elsewhere (50%–70%) [46–48], indicating good rate capability. In addition, no significant IR drop was observed in the GCD curves, indicating low internal resistance. In Fig. 4(e), the low internal resistance was also reflected in EIS, where R_s and R_{ct} were found to be 1.37 and 0.89 Ω, respectively (Fig. S9 and Table S2 in the ESM). Moreover, MoS_2/PANI-I@C-3nm delivered a characteristic frequency, f_0, of 0.44 Hz at a phase angle of –45° (Fig. 4(f)), marking the point where the resistive and capacitive impedances are equal and corresponds to a small time constant, τ (f_0^{-1}), of 2.25 s. This value was substantially smaller than the results of the activated carbon-based electrocapacitors reported (10 s) [49, 50]. Again, the rapid frequency response confirms the outstanding ion transport capability of MoS_2/PANI-I@C-3nm.

The prominent performance improvement observed in MoS_2/PANI-I@C-3nm is related to the small charge transfer resistance. This arises from the good conductivity of both PANI and MoS_2 monolayers, which contain high concentrations of 1T phase, and the large electrochemically active surface of PANI grown on the MoS_2 monolayers. Furthermore, the improved capacitance of MoS_2/PANI-I@C-3nm, compared to MoS_2/PANI-I without the carbon coating at the same scan rate (563 F·g^{-1} at 1 A·g^{-1}, Fig. 5(b)), can also be

attributed to the enhanced conductivity and porous structure from the carbon shell, which do not cause additional contact resistance but can facilitate rapid interfacial charge transfer through the electrode and allow for more charge storage as a conductive network [28, 44]. This can be verified by the larger R_s and R_{ct}

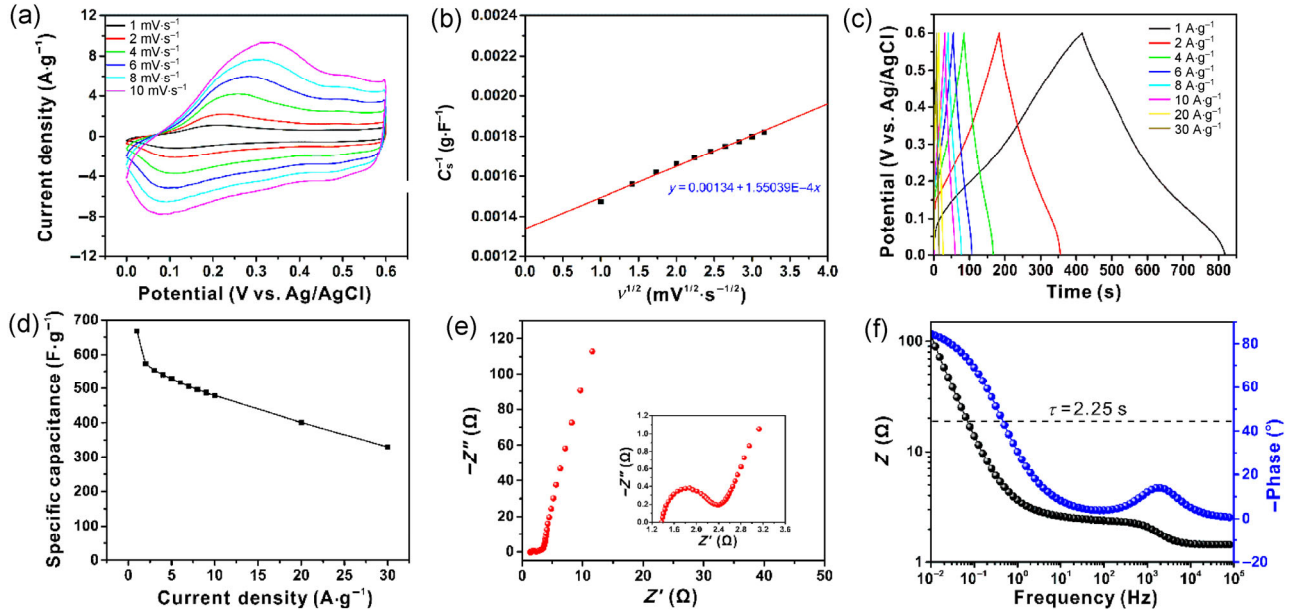

Figure 4 Electrochemical properties of MoS_2/PANI-I@C-3nm. (a) Cyclic voltammetry curves at various scan rates (1–10 mV·s^{-1}). (b) Plot of the reciprocal of the specific capacitance (C_s^{-1}) as a function of the square root of the scan rate ($v^{1/2}$). (c) Galvanostatic charge/discharge curves. (d) Specific capacitance at various current densities (1–30 A·g^{-1}). (e) Nyquist plot. (f) Bode plot. The dashed line highlights the characteristic frequency, f_0 (τ^{-1}), at the phase angle of –45°.

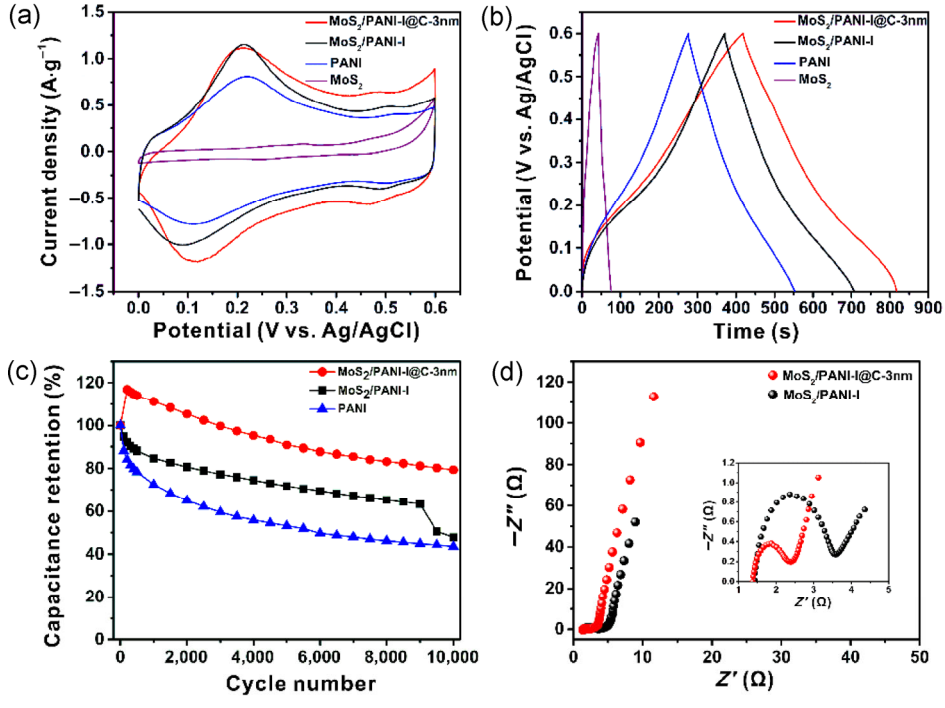

Figure 5 (a) CV curves of MoS_2/PANI-I@C-3nm, MoS_2/PANI-I, PANI and MoS_2 at a scan rate of 1 mV·s^{-1}. (b) GCD curves of MoS_2/PANI-I@C-3nm, MoS_2/PANI-I, PANI and MoS_2 at a current density of 1 A·g^{-1}. (c) Cycling performance of MoS_2/PANI-I, MoS_2/PANI-I@C-3nm and bare PANI electrodes. (d) EIS of MoS_2/PANI-I and MoS_2/PANI-I@C-3nm.

for MoS_2/PANI-I, i.e., 1.50 and 2.08 Ω, respectively (Fig. 5(d) and Table S2 in the ESM).

More significantly, the MoS_2/PANI-I@C-3nm electrode also exhibited exceptional cycle stability. As shown in Fig. 5(c), ~80% capacitance retention after 10,000 cycles was observed, which was much higher than that of the bare PANI (44%). This shows that the carbon-coated organic–inorganic nanostructures of PANI and MoS_2 monolayers can enhance the specific capacitance and cycle stability. In addition to the synergic effects that arise from interfacial contact between the PANI nanostructures and MoS_2 monolayers and effectively enhance the cycling stability, the optimized carbon layer, which can bear the volumetric fluctuations and serve as a conductive network to hold the electrode fragments together, plays a significant role in stabilizing the structure of the MoS_2/PANI-I@C-3nm electrodes during charge/discharge cycling, and realizing excellent capability retention. This was confirmed by the more stable performance of the ~3 nm carbon coated MoS_2/PANI-I@C-3nm than that of MoS_2/PANI-I without the carbon layers (48%) (Fig. 5(c)). The TEM image of MoS_2/PANI-I@C-3nm (Fig. S10 in the ESM) confirms the stable structures without obvious pulverization after being tested for 10,000 cycles.

Moreover, the same tests were also performed for the other carbon layer-coated composites, i.e., ~5 nm carbon coated MoS_2/PANI-I@C-5nm and ~9 nm carbon-coated MoS_2/PANI-I@C-9nm, which were synthesized by a hydrothermal treatment for 4 h and using 6 times the glucose relative to that of MoS_2/PANI-I@C-3nm (section 2.3). The increased carbon layer thickness was also confirmed by XPS (Figs. S6(a)–S6(g) in the ESM), where the C=C content (Fig. S6(h) in the ESM) in MoS_2/PANI-I@C-5nm and MoS_2/PANI-I@C-9nm were slightly higher than that of MoS_2/PANI-I@C-3nm. In contrast to MoS_2/PANI-I@C-3nm, the capacitance of MoS_2/PANI-I@C-5nm and MoS_2/PANI-I@C-9nm reached only 279 and 509 $F \cdot g^{-1}$ at 1 $A \cdot g^{-1}$, respectively (Fig. 6(a)). Although the result of MoS_2/PANI-I@C-9nm was superior to that of bare PANI, the 9-nm thick carbon layer probably restrains the diffusion of ions to some degree. In addition, a longer hydrothermal reaction time may also cause the destruction of the hierarchical structure, resulting in a much lower capacitance for MoS_2/PANI-I@C-5nm (Fig. S11 in the ESM). Note that the thicker carbon layer, e.g., 9 nm, gives the MoS_2/PANI-I@C-9nm (Fig. 6(c) and Fig. S12 in the ESM) electrode a capacitance retention of 73%, which is comparable to MoS_2/PANI-I@C-3nm. However, the improved cycling stability was at the expense of the electrochemical performance. On the other hand, longer hydrothermal times improved neither the specific capacitance nor capability retention. For example, the capacitance retention of MoS_2/PANI@C-5nm was only 30% (Fig. 6(c)), and the capacitance was low. These results show that the optimal performance, including high specific capacitance and good cycling stability of the MoS_2/PANI@C nanohybrids would be based on the appropriate thickness of the carbon coating and stable structure.

In addition to the thickness of the carbon coating, the content of PANI in MoS_2/PANI hybrid SCs is also important. Both MoS_2/PANI-II@C-3nm (low PANI

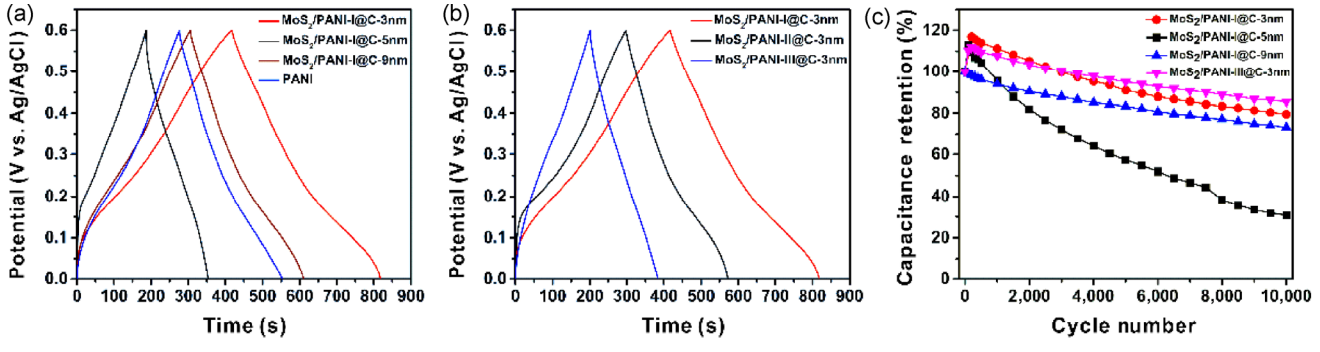

Figure 6 (a) GCD curves of MoS_2/PANI-I@C-3nm, MoS_2/PANI-I@C-5nm, MoS_2/PANI-I@C-9nm and PANI at a current density of 1 $A \cdot g^{-1}$. (b) GCD curves of MoS_2/PANI-I@C-3nm, MoS_2/PANI-II@C-3nm and MoS_2/PANI-III@C-3nm at a current density of 1 $A \cdot g^{-1}$. (c) Cycling performance of MoS_2/PANI-I@C-3nm, MoS_2/PANI-I@C-5nm, MoS_2/PANI-I@C-9nm and MoS_2/PANI-III@C-3nm electrodes.

content) and MoS_2/PANI-III@C-3nm (high PANI content) in Fig. 6(b), Figs. S13 and S14 in the ESM exhibited lower specific capacities than MoS_2/PANI-I@C-3nm. Although MoS_2/PANI-III@C-3nm (Fig. 6(c)) with a PANI content higher than MoS_2/PANI-I@C-3nm has higher capacitance retention (~86%), a much lower specific capacitance was obtained (305 $F \cdot g^{-1}$ at 1 $A \cdot g^{-1}$, Fig. 6(c)), which is related to the additional self-polymerization of PANI occurring out of the MoS_2 monolayers (Fig. S15 in the ESM). Therefore, MoS_2/PANI-I@C-3nm exhibits a much better balance between the specific capacitance and cycle stability, suggesting that it is also critical to optimize the MoS_2 to PANI ratio in the resulting SCs (Figs. S16 and S17 in the ESM).

To evaluate the application potential of MoS_2/PANI-I@C-3nm electrodes, its specific capacitance and cycle stability were compared with those of the conducting polymer-based composite electrodes, as shown in Fig. 7 and Table S3 in the ESM. To the best of the authors' knowledge, there are hardly any pseudocapacitive electrodes based on conducting polymers in an aqueous electrolyte that can achieve a specific capacitance > 700 $F \cdot g^{-1}$ and a capacitance retention of ~80% after 10,000 cycles. Its comprehensive electrochemical performance was also superior to that of the SCs based on PPy deposited on MoS_2 (698 $F \cdot g^{-1}$ at 0.5 $A \cdot g^{-1}$ and the 85% cycle retention after 4,000 cycles) [28]. The remarkable specific capacitance, cycle stability and good rate capacity may be attributed to the good conductivity of the doped PANI and metallic 1T phase of MoS_2 monolayers, large electrochemically active surface areas and small resistance for charge transfer as well as the reduced ion diffusion length by interfacial contact between PANI and MoS_2 monolayers. More importantly, a properly thin carbon shell plays a significant role in enhancing the charge transport efficiency and stabilizing the nanostructure.

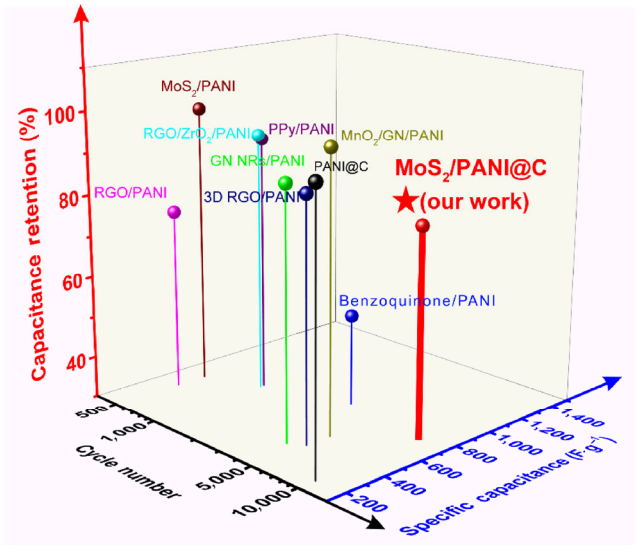

Figure 7 Performance comparison of the specific capacitance and cycle stability among the PANI-based electrodes. (PPy/PANI [22], reduced graphene oxide (RGO)/PANI [39], 3D RGO/PANI [41], PANI@C [44], graphene nanoribbons (GN NRs)/PANI [51], Benzoquinone/PANI [52], MoS_2/PANI [43], RGO/ZrO_2/PANI [53], MnO_2/GN/PANI [40]). Most results were collected in three-electrode cells, RGO/ZrO_2/PANI used a glassy carbon electrode as the working electrode and RGO/PANI and 3D RGO/PANI were measured in two-electrode cells.

4 Conclusions

The deposition of PANI on MoS_2 monolayers with more than 70% 1T phase can result in a synergic effect and achieve significant performance improvement as electrodes in SCs. A thin carbon layer on the MoS_2/PANI nanohybrids contributes further to enhancing the specific capacitance and cycle stability of the SC electrodes. By tuning the PANI content and the thickness of the carbon layers, MoS_2/PANI-I@C-3nm with a ~3 nm thin carbon layer exhibited a specific capacitance >700 $F \cdot g^{-1}$ and 80% capacitance retention after 10,000 cycles, which has not been reported in previous studies related to conducting polymer-based SC electrodes. The general strategy reported here is expected to open a new avenue to improving the comprehensive performance of polymer-based pseudocapacitive electrodes.

Acknowledgements

We are grateful for financial support from Fudan University, National Basic Research Program of China (No. 2011CB605702), National Natural Science Foundation of China (No. 51173027), The Program for Professor of Special Appointment (Eastern Scholar) at Shanghai Institutions of Higher Learning (No. TP2015002) and Shanghai Basic Research Program

(No. 14JC1400600). We also thank Miss Q. Yan, Dr. L. Dei, Dr. G. Qi, Dr. Y. Cui and Dr. Y. Ren at Fudan University and Miss Q. Hu at Shanghai Jiao Tong University for the help with the experiments. Dr. S. Ye and Dr. Y. Zhang at Fudan University provide some suggestions, too. I. S. would like to extend his sincere appreciation to the Deanship of Scientific Research at the King Saud University for its funding of this research through the Research Prolific Research Group, Project No PRG-1436-25.

Electronic Supplementary Material: Supplementary material (experimental section including preparing MoS_2 and determining the thickness of carbon shells etc.; supporting figures containing Zeta potential, Raman, TGA measurements and performance comparisons etc.) is available in the online version of this article at http://dx.doi.org/10.1007/s12274-016-0983-3.

References

[1] Simon, P.; Gogotsi, Y. Materials for electrochemical capacitors. *Nat. Mater.* **2008**, *7*, 845–854.

[2] Xu, Y. X.; Shi, G. Q.; Duan, X. F. Self-assembled three-dimensional graphene macrostructures: Synthesis and applications in supercapacitors. *Acc. Chem. Res.* **2015**, *48*, 1666–1675.

[3] Yu, D. S.; Goh, K.; Wang, H.; Wei, L.; Jiang, W. C.; Zhang, Q.; Dai, L. M.; Chen, Y. Scalable synthesis of hierarchically structured carbon nanotube-graphene fibres for capacitive energy storage. *Nat. Nanotechnol.* **2014**, *9*, 555–562.

[4] Augustyn, V.; Simon, P.; Dunn, B. Pseudocapacitive oxide materials for high-rate electrochemical energy storage. *Energy Environ. Sci*. **2014**, *7*, 1597–1614.

[5] Hercule, K. M.; Wei, Q. L.; Khan, A. M.; Zhao, Y. L.; Tian, X. C.; Mai, L. Q. Synergistic effect of hierarchical nanostructured MoO_2/$Co(OH)_2$ with largely enhanced pseudocapacitor cyclability. *Nano Lett.* **2013**, *13*, 5685–5691.

[6] Yang, C.; Dong, L.; Chen, Z. X.; Lu, H. B. High-performance all-solid-state supercapacitor based on the assembly of graphene and manganese (II) phosphate nanosheets. *J. Phys. Chem. C* **2014**, *118*, 18884–18891.

[7] Zhao, S. L.; Yin, H. J.; Du, L.; He, L. C.; Zhao, K.; Chang, L.; Yin, G. P.; Zhao, H. J.; Liu, S. Q.; Tang, Z. Y. Carbonized nanoscale metal–organic frameworks as high performance electrocatalyst for oxygen reduction reaction. *ACS Nano* **2014**, *8*, 12660–12668.

[8] Choi, K. M.; Jeong, H. M.; Park, J. H.; Zhang, Y. B.; Kang, J. K.; Yaghi, O. M. Supercapacitors of nanocrystalline metal–organic frameworks. *ACS Nano* **2014**, *8*, 7451–7457.

[9] Yin, H. J.; Zhao, S. L.; Zhao, K.; Muqsit, A.; Tang, H. J.; Chang, L.; Zhao, H. J.; Gao, Y.; Tang, Z. Y. Ultrathin platinum nanowires grown on single-layered nickel hydroxide with high hydrogen evolution activity. *Nat. Commun.* **2015**, *6*, 6430.

[10] Feng, L. D.; Zhu, Y. F.; Ding, H. Y.; Ni, C. Y. Recent progress in nickel based materials for high performance pseudocapacitor electrodes. *J. Power Sources* **2014**, *267*, 430–444.

[11] Yin, H. J.; Zhao, S. L.; Wan, J. W.; Tang, H. J.; Chang, L.; He, L. C.; Zhao, H. J.; Gao, Y.; Tang, Z. Y. Three-dimensional graphene/metal oxide nanoparticle hybrids for high-performance capacitive deionization of saline water. *Adv. Mater.* **2013**, *25*, 6270–6276.

[12] Cao, X. H.; Yin, Z. Y.; Zhang, H. Three-dimensional graphene materials: Preparation, structures and application in supercapacitors. *Energy Environ. Sci.* **2014**, *7*, 1850–1865.

[13] Wang, D.-W.; Li, F.; Zhao, J. P.; Ren, W. C.; Chen, Z.-G.; Tan, J.; Wu, Z.-S.; Gentle, I.; Lu, G. Q.; Cheng, H.-M. Fabrication of graphene/polyaniline composite paper via *in situ* anodic electropolymerization for high-performance flexible electrode. *ACS Nano* **2009**, *3*, 1745–1752.

[14] Xu, J. J.; Wang, K.; Zu, S. Z.; Han, B. H.; Wei, Z. X. Hierarchical nanocomposites of polyaniline nanowire arrays on graphene oxide sheets with synergistic effect for energy storage. *ACS Nano* **2010**, *4*, 5019–5026.

[15] Wu, Q.; Xu, Y. X.; Yao, Z. Y.; Shi, G. Q. Supercapacitors based on flexible graphene/polyaniline nanofiber composite films. *ACS Nano* **2010**, *4*, 1963–1970.

[16] Zhao, Y.; Liu, B. R.; Pan, L. J.; Yu, G. H. 3D nanostructured conductive polymer hydrogels for high-performance electrochemical devices. *Energy Environ. Sci*. **2013**, *6*, 2856–2870.

[17] Wang, K.; Wu, H. P.; Meng, Y. N.; Wei, Z. X. Conducting polymer nanowire arrays for high performance supercapacitors. *Small* **2014**, *10*, 14–31.

[18] Xia, C.; Chen, W.; Wang, X. B.; Hedhili, M. N.; Wei, N. N.; Alshareef, H. N. Highly stable supercapacitors with conducting polymer core–shell electrodes for energy storage applications. *Adv. Energy Mater.* **2015**, *5*, 1401805.

[19] Kim, B. C.; Kwon, J. S.; Ko, J. M.; Park, J. H.; Too, C. O.; Wallace, G. G. Preparation and enhanced stability of flexible supercapacitor prepared from Nafion/polyaniline nanofiber. *Synthetic Met.* **2010**, *160*, 94–98.

[20] Fan, W.; Zhang, C.; Tjiu, W. W.; Pramoda, K. P.; He, C. B.; Liu, T. X. Graphene-wrapped polyaniline hollow spheres as novel hybrid electrode materials for supercapacitor

applications. *ACS Appl. Mater. Interfaces* **2013**, *5*, 3382–3391.

[21] Jiang, H.; Ma, J.; Li, C. Z. Polyaniline–MnO_2 coaxial nanofiber with hierarchical structure for high-performance supercapacitors. *J. Mater. Chem.* **2012**, *22*, 16939–16942.

[22] Wang, Z. L.; He, X. J.; Ye, S. H.; Tong, Y. X.; Li, G. R. Design of polypyrrole/polyaniline double-walled nanotube arrays for electrochemical energy storage. *ACS Appl. Mater. Interfaces* **2014**, *6*, 642–647.

[23] Chen, D.; Tang, L. H.; Li, J. H. Graphene-based materials in electrochemistry. *Chem. Soc. Rev.* **2010**, *39*, 3157–3180.

[24] Zhang, L. L.; Zhao, X.; Stoller, M. D.; Zhu, Y. W.; Ji, H. X.; Murali, S.; Wu, Y. P.; Perales, S.; Clevenger, B.; Ruoff, R. S. Highly conductive and porous activated reduced graphene oxide films for high-power supercapacitors. *Nano Lett.* **2012**, *12*, 1806–1812.

[25] Soon, J. M.; Loh, K. P. Electrochemical double-layer capacitance of MoS_2 nanowall films. *Electrochem. Solid-State Lett.* **2007**, *10*, A250–A254.

[26] Gopalakrishnan, K.; Sultan, S.; Govindaraj, A.; Rao, C. N. R. Supercapacitors based on composites of PANI with nanosheets of nitrogen-doped RGO, $BC_{1.5}N$, MoS_2 and WS_2. *Nano Energy* **2015**, *12*, 52–58.

[27] Acerce, M.; Voiry, D.; Chhowalla, M. Metallic 1T phase MoS_2 nanosheets as supercapacitor electrode materials. *Nat. Nanotechnol.* **2015**, *10*, 313–318.

[28] Tang, H. J.; Wang, J. Y.; Yin, H. J.; Zhao, H. J.; Wang, D.; Tang, Z. Y. Growth of polypyrrole ultrathin films on MoS_2 monolayers as high-performance supercapacitor electrodes. *Adv. Mater.* **2015**, *27*, 1117–1123.

[29] Hao, C. X.; Wen, F. S.; Xiang, J. Y.; Wang, L. M.; Hou, H.; Su, Z. B.; Hu, W. T.; Liu, Z. Y. Controlled incorporation of $Ni(OH)_2$ nanoplates into flowerlike MoS_2 nanosheets for flexible all-solid-state supercapacitors. *Adv. Funct. Mater.* **2014**, *24*, 6700–6707.

[30] Lukatskaya, M. R.; Mashtalir, O.; Ren, C. E.; Dall'Agnese, Y.; Rozier, P.; Taberna, P. L.; Naguib, M.; Simon, P.; Barsoum, M. W.; Gogotsi, Y. Cation intercalation and high volumetric capacitance of two-dimensional titanium carbide. *Science* **2013**, *341*, 1502–1505.

[31] Chhowalla, M.; Shin, H. S.; Eda, G.; Li, L. J.; Loh, K. P.; Zhang, H. The chemistry of two-dimensional layered transition metal dichalcogenide nanosheets. *Nat. Chem.* **2013**, *5*, 263–275.

[32] Shen, J. F.; He, Y. M.; Wu, J. J.; Gao, C. T.; Keyshar, K.; Zhang, X.; Yang, Y. C.; Ye, M. X.; Vajtai, R.; Lou, J. et al. Liquid phase exfoliation of two-dimensional materials by directly probing and matching surface tension components. *Nano Lett.* **2015**, *15*, 5449–5454.

[33] Heising, J.; Kanatzidis, M. G. Exfoliated and restacked MoS_2 and WS_2: Ionic or neutral species? Encapsulation and ordering of hard electropositive cations. *J. Am. Chem. Soc.* **1999**, *121*, 11720–11732.

[34] Joensen, P.; Crozier, E. D.; Alberding, N.; Frindt, R. F. A study of single-layer and restacked MoS_2 by X-ray diffraction and X-ray absorption spectroscopy. *J. Phys. C* **1987**, *20*, 4043–4053.

[35] Voiry, D.; Goswami, A.; Kappera, R.; e Silva, C. D. C. C.; Kaplan, D.; Fujita, T.; Chen, M. W.; Asefa, T.; Chhowalla, M. Covalent functionalization of monolayered transition metal dichalcogenides by phase engineering. *Nat. Chem.* **2015**, *7*, 45–49.

[36] Eda, G.; Yamaguchi, H.; Voiry, D.; Fujita, T.; Chen, M. W.; Chhowalla, M. Photoluminescence from chemically exfoliated MoS_2. *Nano Lett.* **2011**, *11*, 5111–5116.

[37] Xu, H. L.; Li, X. W.; Wang, G. C. Polyaniline nanofibers with a high specific surface area and an improved pore structure for supercapacitors. *J. Power Sources* **2015**, *294*, 16–21.

[38] Bai, M. H.; Liu, T. Y.; Luan, F.; Li, Y.; Liu, X. X. Electrodeposition of vanadium oxide-polyaniline composite nanowire electrodes for high energy density supercapacitors. *J. Mater. Chem. A* **2014**, *2*, 10882–10888.

[39] Kim, M.; Lee, C.; Jang. J. Fabrication of highly flexible, scalable, and high-performance supercapacitors using polyaniline/reduced graphene oxide film with enhanced electrical conductivity and crystallinity. *Adv. Funct. Mater.* **2014**, *24*, 2489–2499.

[40] Han, G. Q.; Liu, Y.; Zhang, L. L.; Kan, E. J.; Zhang, S. P.; Tang, J.; Tang, W. H. MnO_2 nanorods intercalating graphene oxide/polyaniline ternary composites for robust high-performance supercapacitors. *Sci. Rep.* **2014**, *4*, 4824.

[41] Meng, Y. N.; Wang, K.; Zhang, Y. J.; Wei, Z. X. Hierarchical porous graphene/polyaniline composite film with superior rate performance for flexible supercapacitors. *Adv. Mater.* **2013**, *25*, 6985–6990.

[42] Yang, L. C.; Wang, S. N.; Mao, J. J.; Deng, J. W.; Gao, Q. S.; Tang, Y.; Schmidt, O. G. Hierarchical MoS_2/polyaniline nanowires with excellent electrochemical performance for lithium-ion batteries. *Adv. Mater.* **2013**, *25*, 1180–1184.

[43] Huang, K.-J.; Wang, L.; Liu, Y.-J.; Wang, H.-B.; Liu, Y.-M.; Wang, L.-L. Synthesis of polyaniline/2-dimensional graphene analog MoS_2 composites for high-performance supercapacitor. *Electrochim. Acta* **2013**, *109*, 587–594.

[44] Liu, T. Y.; Finn, L.; Yu, M. H.; Wang, H. Y.; Zhai, T.; Lu, X. H.; Tong, Y. X.; Li, Y. Polyaniline and polypyrrole pseudocapacitor electrodes with excellent cycling stability.

Nano Lett. **2014**, *14*, 2522–2527.

[45] Ardizzone, S.; Fregonara, G.; Trasatti, S. "Inner" and "outer" active surface of RuO_2 electrodes. *Electrochim. Acta* **1990**, *35*, 263–267.

[46] Wang, Y. C.; Zhou, T.; Jiang, K.; Da, P. M.; Peng, Z.; Tang, J.; Kong, B.; Cai, W.-B.; Yang, Z. Q.; Zheng, G. F. Reduced mesoporous Co_3O_4 nanowires as efficient water oxidation electrocatalysts and supercapacitor electrodes. *Adv. Energy Mater.* **2014**, *4*, 1400696.

[47] Shen, L. F.; Wang, J.; Xu, G. Y.; Li, H. S.; Dou, H.; Zhang, X. G. $NiCo_2S_4$ nanosheets grown on nitrogen-doped carbon foams as an advanced electrode for supercapacitors. *Adv. Energy Mater.* **2015**, *5*, 1400977.

[48] Cong, H.-P.; Ren, X.-C.; Wang, P.; Yu, S.-H. Flexible graphene-polyaniline composite paper for high-performance supercapacitor. *Energy Environ. Sci.* **2013**, *6*, 1185–1191.

[49] Taberna, P. L.; Simon, P.; Fauvarque, J. F. Electrochemical characteristics and impedance spectroscopy studies of carbon–carbon supercapacitors. *J. Electrochem. Soc.* **2003**, *150*, A292–A300.

[50] El-Kady, M. F.; Strong, V.; Dubin, S.; Kaner, R. B. Laser scribing of high-performance and flexible graphene-based electrochemical capacitors. *Science* **2012**, *335*, 1326–1330.

[51] Li, L.; Raji, A. R. O.; Fei, H. L.; Yang, Y.; Samuel, E. L. G.; Tour, J. M. Nanocomposite of polyaniline nanorods grown on graphene nanoribbons for highly capacitive pseudocapacitors. *ACS Appl. Mater. Interfaces* **2013**, *5*, 6622–6627.

[52] Vonlanthen, D.; Lazarev, P.; See, K. A.; Wudl, F.; Heeger, A. J. A stable polyaniline-benzoquinone-hydroquinone supercapacitor. *Adv. Mater.* **2014**, *26*, 5095–5100.

[53] Giri, S.; Ghosh, D.; Das, C. K. Growth of vertically aligned tunable polyaniline on graphene/ZrO_2 nanocomposites for supercapacitor energy-storage application. *Adv. Funct. Mater.* **2014**, *24*, 1312–1324.